EDGE ARTICLE

Thermodynamic and kinetic studies of H₂ and N₂ binding to bimetallic nickel-group 13 complexes and neutron structure of a Ni(η²-H₂) adduct†

Ryan C. Cammarota,‡[a] Jing Xie, [iD] ‡[abe] Samantha A. Burgess, [iD][c]
Matthew V. Vollmer,[a] Konstantinos D. Vogiatzis, [iD][abf] Jingyun Ye, [iD][ab]
John C. Linehan, [iD][c] Aaron M. Appel, [iD][c] Christina Hoffmann, [iD][d] Xiaoping Wang, [iD][d]
Victor G. Young, Jr.[a] and Connie C. Lu *[a]

Understanding H₂ binding and activation is important in the context of designing transition metal catalysts for many processes, including hydrogenation and the interconversion of H₂ with protons and electrons. This work reports the first thermodynamic and kinetic H₂ binding studies for an isostructural series of first-row metal complexes: NiML, where M = Al (**1**), Ga (**2**), and In (**3**), and L = [N(*o*-(NCH₂P^{i}Pr₂)C₆H₄)₃]³⁻. Thermodynamic free energies (ΔG°) and free energies of activation (ΔG‡) for binding equilibria were obtained *via* variable-temperature ³¹P NMR studies and lineshape analysis. The supporting metal exerts a large influence on the thermodynamic favorability of both H₂ and N₂ binding to Ni, with ΔG° values for H₂ binding found to span nearly the entire range of previous reports. The non-classical H₂ adduct, (η²-H₂)NiInL (**3**-H₂), was structurally characterized by single-crystal neutron diffraction—the first such study for a Ni(η²-H₂) complex or any d¹⁰ M(η²-H₂) complex. UV-Vis studies and TD-DFT calculations identified specific electronic structure perturbations of the supporting metal which poise NiML complexes for small-molecule binding. ETS-NOCV calculations indicate that H₂ binding primarily occurs *via* H–H σ-donation to the Ni 4p$_z$-based LUMO, which is proposed to become energetically accessible as the Ni(0)→M(III) dative interaction increases for the larger M(III) ions. Linear free-energy relationships are discussed, with the activation barrier for H₂ binding (ΔG‡) found to decrease proportionally for more thermodynamically favorable equilibria. The ΔG° values for H₂ and N₂ binding to NiML complexes were also found to be more exergonic for the larger M(III) ions.

Introduction

Developing homogeneous base metal catalysts which can activate H₂ and selectively mediate catalytic hydrogenation, H₂ oxidation, and proton reduction have been active areas of research in recent years.[1–5] In such processes, the strength of H₂ binding, the interplay between σ-donation (H₂ σ → M) and π-back-donation (M → H₂ σ*), the resulting extent of H–H activation, and the ease of generating reactive M–H species all can play a critical role in determining catalytic activity and selectivity. H₂ activation is typically initiated by side-on binding of H₂ to form a M(η²-H₂) adduct, which precedes the generation of reactive M–H species *via* subsequent oxidative addition or deprotonation events.[6–8] Despite the ubiquity of H₂ binding as a key fundamental reaction step in catalysis,[9] limited experimental data has been reported regarding the thermodynamic and kinetic favorability of H₂ binding to transition metals, especially for the first-row transition metals.[6–8] To the best of our knowledge, thermodynamic H₂-binding data have only been reported for a handful of first-row metal complexes: Cr(PCy₃)₂(CO)₃,[10,11] [Mn(CO)(dppe)₂]⁺,[12] [Fe(P₄N₂)]⁺,[13] and Co(TPB),[14] where dppe is bis(diphenylphosphino)ethane, P₄N₂ is a tetraphosphine with two pendant amines, and TPB is tris(*o*-diisopropylphosphinophenyl)borane. Moreover, without a series of similar M(η²-H₂) adducts with which to compare

ᵃDepartment of Chemistry, University of Minnesota-Twin Cities, 207 Pleasant Street SE, Minneapolis, Minnesota 55455, USA. E-mail: clu@umn.edu

ᵇSupercomputing Institute, Chemical Theory Center, University of Minnesota-Twin Cities, 207 Pleasant Street SE, Minneapolis, Minnesota 55455, USA

ᶜCatalysis Science Group, Pacific Northwest National Laboratory, P. O. Box 999, MS K2-57, Richland, Washington 99352, USA

ᵈNeutron Scattering Division, Oak Ridge National Laboratory, Oak Ridge, Tennessee 37831, USA

ᵉKey Laboratory of Cluster Science of Ministry of Education, School of Chemistry and Chemical Engineering, Beijing Institute of Technology, Beijing 100081, China

ᶠDepartment of Chemistry, University of Tennessee, Knoxville, Tennessee 37996, USA

‡ These authors contributed equally.

thermodynamic data, the understanding gained by quantifying H_2 binding to a single metal complex are relatively limited.

Recently, the double-decker ligand, $[N(o\text{-}(NCH_2P^iPr_2)C_6H_4)_3]^{3-}$ (abbreviated as L), was used to prepare bimetallic (η^2-H_2)M_AM_BL complexes in which group 13 Lewis acidic supporting metal ions (M_B) induce H_2 binding at Ni(0) and Co($-I$) metal centers (M_A).[15,16] Figueroa and Gabbaï have independently shown that appending a Lewis acidic σ-acceptor to a d^{10} transition metal induces binding of a Lewis base donor *trans* to the σ-acceptor.[17–19] We and others have used a tethered σ-acceptor to promote activity at the transition metal for catalytic CO_2 functionalization.[20–22] Here, we report the first thermodynamic and kinetic studies of H_2 binding to a Ni center in an isostructural series, where M_B = Al, Ga, and In. In the case of the In(III) supporting ion, strong H_2 binding allowed for structural elucidation *via* single-crystal neutron diffraction. Significant modulation of the thermodynamic favorability of both H_2 and N_2 binding to Ni was enabled by introducing and varying the group 13 supporting metal ion, with H_2 binding free energies (ΔG°) found to span nearly the entire range of previously reported values. The (η^2-H_2)NiML complexes also exhibit different extents of H–H activation and kinetic rates of H_2 binding and loss. Through a combination of experimental and theoretical studies on binding and electronic structure, we present a comprehensive understanding of how a supporting group 13 metal ion poises a proximal transition metal for small-molecule binding and influences both the thermodynamics and kinetics of binding equilibria.

Results & discussion

Part I. Neutron diffraction study of (η^2-H_2)NiInL and NMR characterization of (η^2-H_2)NiAlL

We have previously reported a series of bimetallic NiML complexes featuring Ni(0)$\rightarrow$M(III) dative bonds (M = Al (**1**), Ga (**2**), and In (**3**)), where larger group 13 ions, Ga and In, promote H_2 binding to formally d^{10} Ni centers.[16] The resulting non-classical H_2 adducts, (η^2-H_2)NiGaL (**2**-H_2) and (η^2-H_2)NiInL (**3**-H_2), were characterized by ^1H NMR spectroscopy techniques. In addition, the remarkable stability of **3**-H_2 allowed for its molecular structure to be determined by single-crystal X-ray diffraction at 123 K.[16] We currently report a single-crystal neutron diffraction study of **3**-H_2 at 100 K (Fig. 1) and the corresponding X-ray structure at 100 K. To our knowledge, **3**-H_2 is the first H_2 adduct of Ni, or of any d^{10} metal, to be structurally characterized by neutron diffraction. To date, only two other Ni(0) H_2-adducts have been reported, $[O(SiH(o\text{-}^iPr_2PC_6H_4)_2)_2]Ni_2(\eta^2\text{-}H_2)_2$ and $[PhB(o\text{-}^iPr_2PC_6H_4)_2]Ni(\eta^2\text{-}H_2)$, both of which were characterized *in situ* at low T.[23,24]

Table 1 displays selected structural parameters for **3**-H_2. Of note, the bond distances for non-hydrogen atoms in the X-ray and neutron structures of **3**-H_2 are essentially identical within experimental error (Table S4†). The Ni–H distances between the two structures are also within error, though the H–H bond length differs by 0.12 Å. The neutron structure, which is more reliable for placement of H atoms, validates an intact H_2 molecule that is bound in side-on fashion to the Ni center. Upon

Fig. 1 Neutron structure of **3**-H_2. Ellipsoids are shown at the 50% probability level, and H atoms (with the exception of H_2) have been omitted for clarity.

H_2 coordination, the Ni–In bond distance increases slightly from 2.457(1) Å in **3** to 2.4789(2) Å in **3**-H_2. The H–H bond length of 0.80(2) Å is slightly elongated relative to that in free H_2 (0.74 Å), but shorter than the solution-state distance of 0.91 Å that was determined based on the J_{HD} coupling constant of **3**-HD.[16] This discrepancy can be attributed to rapid librational motion of H_2 in **3**-H_2, a phenomenon which typically leads to an average contraction of $\sim$0.07 Å in the apparent solid-state H–H bond distance relative to the solution-state distance determined by NMR studies.[7,25–27] Consistent with this attribution, fast H_2 rotation in solution relative to molecular tumbling is also supported by the previously reported T_1 (min) value for the coordinated H_2 ligand of **3**-H_2.[16]

Notably, the Ni–H bond distance is a parameter that neutron diffraction is uniquely able to experimentally evaluate. The two equivalent Ni–H bond lengths of 1.61(2) Å fall on the longer end of the wide range of the Ni–H distances reported for terminal Ni hydrides (*cf.* 1.32 to 1.65 Å).[28] Although direct comparisons are

Table 1 Selected structural metrics for **3**-H_2 from X-ray and neutron studies at 100 K[a]

	3-H_2 (neutron)	**3**-H_2 (X-ray)
H–H	0.80(2)	0.92(3)
Ni–H	1.61(2)	1.58(2)
	1.61(2)	1.65(2)
Ni–In	2.39(2)	2.4789(2)
Ni–P (avg.)	2.26(1)	2.2618(4)
In–N_{amide} (avg.)	2.13(1)	2.115(1)
In–N_{apical}	2.40(2)	2.366(1)
Ni to P_3-plane	0.31	0.29
In to N_3-plane	0.52	0.50

[a] Values in Å (estimated standard deviations in parentheses). See Table 6 for crystallographic details. See Table S4 for a detailed comparison of the X-ray and neutron structures.

sparse due to the rarity of structurally characterized $M(\eta^2-H_2)$ complexes, the M–H and H–H distances in 3-H_2 are both similar to those for $(\eta^2-H_2)Co(TPB)$, which has M–H and H–H distances of 1.66/1.67 Å and 0.83(2) Å, respectively.[29] Short contact distances between the H_2 unit and the hydrogen atoms of the ligand isopropyl phosphine groups were observed in both 3-H_2 and $(\eta^2-H_2)Co(TPB)$, the closest of which were 2.24 Å and 2.10 Å, respectively. These distances are, within error, close to the intermolecular H···H van der Waals distance (2.2 Å).[30]

Previously, no reaction was observed between NiAlL (1) and H_2 (1 atm) at room temperature. Subsequent studies have found that either high H_2 pressure or low T is needed to observe H_2 binding to 1. At 34 atm H_2 and 232 K, a new species was observed by ^{1}H NMR spectroscopy that is assigned as (η^2-H_2)NiAlL (1-H_2) based on a diagnostic resonance for bound H_2 at −1.5 ppm (Fig. S8 and S9†) and a short T_1 (min) value of ≤49(5) ms (500 MHz, THF-d_8; Fig. S10†).[31,32] The ^{1}H NMR spectrum of the HD isotopomer, (η^2-HD)NiAlL (1-HD), which was formed at 213 K under 3.8 atm HD, displayed a characteristic 1 : 1 : 1 triplet for the bound HD ligand, with $J_{HD} = 34.4$ Hz (Fig. S11†).

With the addition of 1-H_2 to complete the isostructural trio of $Ni(\eta^2-H_2)$ complexes, it is apparent that H_2 activation increases as the supporting metal is varied down group 13 from Al to Ga to In, as reflected by the decreasing J_{HD} values (in Hz): 34.4 for 1-HD > 33.2 for 2-HD > 31.7 for 3-HD (at 213 K; Fig. S11†). Thus, the corresponding estimated solution-state H–H bond distances increase as the supporting metal is varied down group 13, from 0.86 Å for 1-H_2, to 0.88 Å for 2-H_2, to 0.91 Å for 3-H_2.[33] The relative extents of H–H bond activation for the (η^2-H_2)NiML complexes are also in accord with those predicted by DFT calculations (Tables S13, S19 and S20†). That 1-H_2 would have the shortest H–H distance of the trio, and the closest to that of free H_2, is suggestive of the weak and labile nature of H_2 binding to 1 relative to H_2 binding to 2 and 3.[6,7] We further note that the isostructural mononuclear Ni complex, NiLH$_3$ (4),[34] does not bind H_2 even under forcing conditions (193 K, 34 atm H_2),[20] which suggests that the supporting metal

plays a pivotal role in inducing H_2 binding and controlling the extent of H_2 activation. Lastly, both 2-H_2 and 3-H_2 exhibit a greater extent of H_2 activation compared to the two other Ni(0) H_2-adducts: $[O(SiH(o-^iPr_2PC_6H_4)_2)_2]Ni_2(\eta^2-H_2)_2$ ($J_{HD} = 34.2$ Hz) and $[PhB(o-^iPr_2PC_6H_4)_2]Ni(\eta^2-H_2)$ ($J_{HD} = 36.5$ Hz).[23,24]

Part II. H_2 and N_2 binding energies for the NiML triad

Intrigued by the varied propensities for binding and activating H_2 enabled by changing a single atom, we set out to understand how the group 13 supporting metal influences the thermodynamics and kinetics of Ni–H_2 binding equilibria. Previously, (η^2-H_2)NiGaL (2-H_2) was generated in situ under 1 atm H_2, but reverted to 2 upon exposure to vacuum or Ar.[16] Because of its reversible H_2 binding at ambient conditions, 2 was an ideal candidate for initiating binding equilibrium studies. Variable-temperature (VT) ^{31}P NMR spectra of 2 in toluene-d_8 under 6.8 atm H_2 displayed a single resonance, which shifted downfield from 42.7 to 56.4 ppm as the temperature was decreased from 368 K to 221 K (Fig. 2a). As a control experiment, the VT NMR profile of 2 under Ar showed a minimal change in the ^{31}P shift ($\Delta\delta < 0.5$ ppm) over a similar T range (Fig. S12 and S13†). Hence, the VT NMR behavior of 2 under an H_2 atmosphere is consistent with an equilibrium between 2 and 2-H_2 that is governed by fast chemical exchange relative to the ^{31}P NMR timescale (202.4 MHz), where the latter is favored at low T and both species are three-fold symmetric in solution.

Analogous VT ^{31}P NMR experiments were also performed for 2 under various H_2 pressures of 1.0, 13.6, and 34 atm (Fig. S1, S14 and S15†). Of note, for all H_2 pressures examined, the same low T convergence of the ^{31}P resonance to ~56.9 ppm was observed at 193 K, which corresponds to the ^{31}P chemical shift of 2-H_2 (Fig. 2b). At high T, the observed ^{31}P chemical shift approaches that of 2, with closer convergence observed at lower H_2 pressures. These observations are consistent with rapid interconversion between 2 and 2-H_2, such that the observed chemical shift ([31]P δ) is the population-weighted average of the chemical shifts of these exchanging species.[35] Thus, the
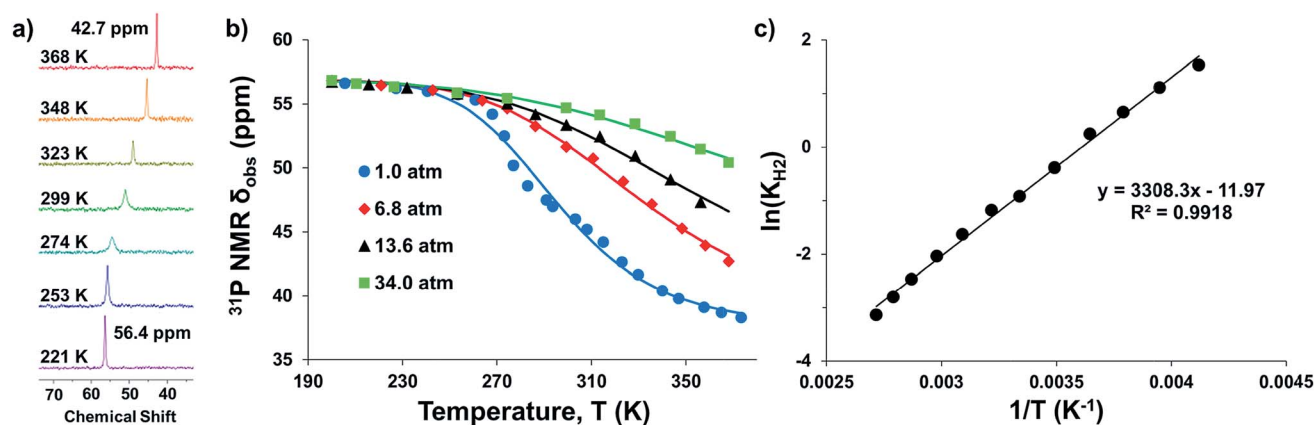

Fig. 2 (a) VT ^{31}P NMR spectra of 2 under 6.8 atm H_2 in toluene-d_8 from 368 to 221 K. (b) Plots of [31]P δ vs. T obtained for various H_2 pressures. Data are shown as points, and solid traces represent the best–fit curves obtained by varying $\Delta H°$ and $\Delta S°$ as parameters (see ESI†). (c) Representative van't Hoff plot of $\ln(K_{H_2})$ vs. $1/T$ at 6.8 atm H_2. The thermodynamic binding parameters shown in Table 2 were determined from van't Hoff plots for data sets collected at 6.8 and 13.6 atm H_2, which exhibit fast chemical exchange.

observed ^{31}P δ can be converted into the equilibrium concentration ratio of **2** and **2**-H_2 (see ESI†). The equilibrium constant for H_2 binding, K_{H_2}, was determined according to eqn (1), where P_{H_2} is the H_2 pressure:

$$K_{H_2} = \frac{[(\eta^2\text{-}H_2)NiML]}{[NiML] \times P_{H_2}} \qquad (1)$$

Next, the thermodynamic parameters for H_2 binding, $\Delta H°$, $\Delta S°$, and $\Delta G°$, were determined using two complementary methods: (1) non-linear fitting of the ^{31}P δ *vs.* T plot in Fig. 2b; and (2) linear regression of the van't Hoff plot of $\ln(K_{H_2})$ *vs.* $1/T$, as shown in Fig. 2c. The analyses were performed using the 6.8 and 13.6 atm datasets, where chemical exchange was rigorously fast relative to the ^{31}P NMR timescale and the variability of ^{31}P δ with T was significant enough to reflect the sampling of an adequate portion of the binding equilibrium. The van't Hoff plot gives $\Delta H°$ = $-6.3(2)$ kcal mol^{-1}, $\Delta S°$ = $-23.0(7)$ cal (mol K)$^{-1}$, and $\Delta G°$ = $+0.6(3)$ kcal mol^{-1} for H_2 binding to **2**, where the standard state conditions are defined as 298 K, 1 atm H_2, and 1 M concentrations of all other species in toluene-d$_8$. Non-linear fitting of the ^{31}P δ *vs.* T plot yields the same thermodynamic values within experimental error (Fig. S16, S17 and Table S2†).

The H_2 binding equilibria for the other NiML complexes, **1** (M = Al) and **3** (M = In), were also investigated by VT ^{31}P NMR spectroscopy. For H_2 binding to **1**, the VT ^{31}P NMR spectra in toluene-d$_8$ (363 to 210 K, 34 atm H_2) show a single ^{31}P resonance shifting downfield relative to that of **1** (30.7 ppm) with decreasing T, and ultimately converging to a chemical shift of $\sim$44.3 ppm for **1**-H_2 (Fig. S18†). The corresponding van't Hoff analysis for H_2 binding to **1** gives $\Delta H°$ = $-6.3(1)$ kcal mol^{-1}, $\Delta S°$ = $-26.4(4)$ cal (mol K)$^{-1}$, and $\Delta G°$ = $+1.6(2)$ kcal mol^{-1} (Fig. S19†). Since **3** binds H_2 strongly, sub-ambient H_2 pressure was necessary to establish a measurable equilibrium between **3** and **3**-H_2 (Fig. S20–S22†). Under 1 atm of 10% H_2 in Ar, where P_{H_2} = 0.1 atm, a single ^{31}P peak was observed from 299 to 357 K (Fig. S20†). However, the lineshapes of the observed ^{31}P peaks are noticeably broadened, which indicates that chemical

exchange between **3** and **3**-H_2 falls into the fast-intermediate regime relative to the ^{31}P NMR timescale.[36] This is problematic because non-Lorentzian lineshapes and exchange broadening may diminish the reliability of the thermodynamic parameters determined under fast-intermediate exchange conditions.[37] Hence, we caution that the thermodynamic values for H_2 binding to **3**, $\Delta H°$ = $-14.8(6)$ kcal mol^{-1}, $\Delta S°$ = $-37(2)$ cal mol^{-1} K^{-1}, and $\Delta G°$ = $-3.7(7)$ kcal mol^{-1} (Fig. S23† and Table 2), should be treated as estimates.

To assess the reliability of this estimated $\Delta G°$ value, a control experiment was performed on **2** under identical conditions with 0.1 atm H_2, which showed similarly broad ^{31}P peaks due to fast-intermediate chemical exchange (Fig. S24 and S25†). Comparing the binding parameters obtained for **2** under 0.1 atm H_2 to those obtained under rigorously fast exchange conditions (6.8 and 13.6 atm H_2), we find that the thermodynamic favorability of H_2 binding was overestimated by 0.7 kcal mol^{-1} using the 0.1 atm H_2 dataset. Thus, by applying this 0.7 kcal mol^{-1} empirical correction, we propose that a better $\Delta G°$ estimate for H_2 binding to **3** is $-3.0(7)$ kcal mol^{-1}. In support, lineshape simulations of VT ^{31}P NMR spectra of **3** under 1 atm H_2 independently gives $\Delta G°$ = $-2.3(2)$ kcal mol^{-1}, which is within experimental error of the corrected value of $-3.0(7)$ kcal mol^{-1} (Fig. S26†).

Next, we sought to investigate the related equilibria of N_2 binding to the NiML complexes using VT ^{31}P NMR experiments. The equilibrium between **2** and **2**-N_2 was monitored at 1 atm N_2 and low T (226 to 193 K). Distinct ^{31}P resonances were observed for both **2** and **2**-N_2 (Fig. S30†), which is characteristic of slow chemical exchange relative to the ^{31}P NMR timescale (161.9 MHz). Quantitative integration of the ^{31}P NMR peaks for **2** and **2**-N_2 allowed for a straightforward determination of K_{N_2} using eqn (2), where P_{N_2} is the N_2 pressure:

$$K_{N_2} = \frac{[(N_2)NiML]}{[NiML] \times P_{N_2}} \qquad (2)$$

Conversely, the interconversion of **3** and **3**-N_2 is fast relative to the ^{31}P NMR timescale (161.9 MHz) at 1 atm N_2 and T > 288 K (Fig. S6 and S31†). As such, the observed chemical shift of the single ^{31}P NMR resonance represents the population-weighted average of the chemical shifts of **3** and **3**-N_2, and the VT NMR data were analyzed as previously described for H_2 binding to **2** (Fig. S31 and S32†). Lastly, the observed equilibrium between **1** and **1**-N_2 at 51 atm N_2 switches from slow exchange at low T ($\leq$210 K) to fast exchange at higher T ($\geq$243 K) (Fig. S33†). Thus, K_{N_2} was evaluated based on the distinct ^{31}P NMR peak integrations for **1** and **1**-N_2 at low T, and based on the observed ^{31}P chemical shift at high T. The thermodynamic binding parameters for the H_2 and N_2 binding equilibria of the NiML complexes are compiled in Tables 2 and 3. Additionally, DFT calculations using the M06-L[38]/bs1 method correctly predict the experimental trends in both the H_2 and N_2 binding free energies for the trio of NiML complexes (Tables 2 and 3).

Across the NiML series, $\Delta G°$ for both H_2 and N_2 binding was modulated by $\sim$5 kcal mol^{-1}, with increasing thermodynamic favorability for both H_2 and N_2 binding observed as the

Table 2 Experimental and DFT-calculated H_2 thermodynamic binding parameters for **1**, **2**, and **3**[a]

	1	**2**[b]	**3**
$\Delta H°$ (kcal mol^{-1})	$-6.3(1)$	$-6.3(2)$	$-14.8(6)$[d]
$\Delta S°$ (cal mol^{-1} K^{-1})	$-26.4(4)$	$-23.0(7)$	$-37(2)$[d]
$\Delta G°$ (kcal mol^{-1})	$1.6(2)$	$0.6(3)$	$-3.7(7)$[d]
			$-3.0(7)$[e]
$\Delta G°$ (DFT)[c]	2.8	0.9	-1.9

[a] Standard deviations obtained from van't Hoff linear regression analyses are given in parentheses. Standard state is defined as 298 K, 1 atm H_2 (or N_2), and 1 M of all other species in toluene-d$_8$. [b] H_2 binding studies have also been conducted for **2** in THF (Fig. S27–S29): $\Delta G°$ = $+0.1(1)$ kcal mol^{-1}, $\Delta H°$ = $-7.5(1)$ kcal mol^{-1}, and $\Delta S°$ = $-25.4(1)$ cal mol^{-1} K^{-1}. [c] Units of kcal mol^{-1}, see Computational methods in Experimental section for details. [d] Estimated values extracted from fast-intermediate exchange regime data (Fig. S20–S23). [e] Corrected $\Delta G°$ value of $-3.0(7)$ kcal mol^{-1} is likely a better estimate. See text for explanation of the $+0.7$ kcal mol^{-1} correction term.

Table 3 Experimental and DFT-calculated N_2 thermodynamic binding parameters for **1**, **2**, and **3**[a]

	1	**2**	**3**
$\Delta H°$ (kcal mol^{-1})	−4.7(2)	−4.7(3)	−14.5(3)
$\Delta S°$ (cal mol^{-1} K^{-1})	−27.5(5)	−23(1)	−45(1)
$\Delta G°$ (kcal mol^{-1})	3.5(3)	2.1(5)	−1.2(4)
$\Delta G°$ (DFT)[b]	6.3	3.6	0.2

[a] Same as Table 2 footnote a. [b] Same as Table 2 footnote c.

supporting metal was varied down group 13 (Tables 2 and 3). Notably, $\Delta G°$ values for H_2 binding to the NiML complexes nearly span the entire range of previously reported values (from −2 to +3 kcal mol; Tables S6 and S7†). This is remarkable considering that the full range of literature $\Delta G°$ values encompasses H_2 binding to various transition metals (*e.g.* Cr, Mo, W, Re, Fe, Ru, Co, and Ir) in diverse ligand environments.[10,11,13,14,39–45] In contrast, the NiML trio features an isostructural Ni site within the same ligand framework, where the primary difference is the identity of the group 13 metal. We hypothesize that the strength of the Ni(0)→M(III) dative interaction directly tunes the binding at Ni in the position *trans* to M(III), where greater Ni(0)→M(III) interactions lead to stronger small-molecule binding. This hypothesis is generally consistent with other literature examples wherein the interaction of a σ-acceptor with a d^{10} transition metal enhances donor-binding at the *trans* position.[17–19] DFT calculations predict that supporting Ni with In(III) in **3** increases the favorability of H_2 binding by ~8 kcal mol^{-1} relative to NiLH$_3$ (**4**), which are the two limiting extremes in this series (Table S16†).

To the best of our knowledge, (η^2-H_2)Co(TPB) and [(η^2-H_2)Re(CN^{t}Bu)$_3$(PCy$_3$)$_2$]$^+$ were previously reported to have the most favorable H_2 binding free energies, with $\Delta G°_{1\,M} = -4.8(9)$ and −4.8(1.3) kcal mol^{-1}, respectively (Table S7†).[14,39] Notably, **3** binds H_2 even more favorably, with $\Delta G°_{1\,M} \sim -6.5(7)$ kcal mol^{-1}, which was obtained by converting $\Delta G°$ at $P_{H_2} = 1$ atm to $\Delta G°$ for [H_2] = 1 M. In addition, the determination of both H_2 and N_2 binding energies for first-row transition metal complexes is rare.[10,11,13,14,46] Across the NiML series, the binding free energies for H_2 are more favorable than those for N_2 by 1.9(4), 1.5(5), and ~1.8(8) kcal mol^{-1} for **1**, **2**, and **3**, respectively (Tables 2 and 3). A similar trend was reported for [Fe(P$_4$N$_2$)]$^+$ and Cr(CO)$_3$(PCy$_3$)$_2$, whereas $\Delta G°_{1\,M}$ energies for H_2 and N_2 binding to Co(TPB) are identical within error (Tables S6–S9†). The finding that N_2 binding is more competitive with H_2 binding for Co(TPB) than it is for NiML complexes is consistent with the greater π-basicity of low-valent Co toward N_2.[47,48]

In further examining the $\Delta H°$ and $\Delta S°$ contributions for binding to NiML (**1–3**), the large negative $\Delta S°$ values for H_2 and N_2 binding reflect the entropic cost of binding a gas molecule (Tables 2 and 3). In general, a greater entropic cost was observed for N_2 binding than for H_2 binding; this trend can be explained in part by the larger absolute entropy of N_2 relative to H_2.[11] It is also striking that both H_2 and N_2 binding to **3** are considerably more exothermic ($\Delta\Delta H° \approx -9$ kcal mol^{-1}) and entropically

costly ($\Delta\Delta S° \approx -13$ and −20 cal mol^{-1} K^{-1}, respectively) compared with binding to **1** and **2** (Tables 2 and 3). The fact that binding to **3** has the most favorable enthalpic and most unfavorable entropic terms is consistent with tighter and more rigid binding of both H_2 and N_2. Intriguingly, because **1** and **2** have identical $\Delta H°$ values for both H_2 and N_2 binding, the differences in their observed binding propensities originate from the differences in $\Delta S°$ values.

Part III. Kinetics of self-exchange for NiML and (η^2-H_2)NiML complexes

To understand the dependence of the kinetics of the H_2 binding process on the supporting metal, VT ^{31}P NMR lineshape simulations of NiML under 1 atm H_2 were performed to extract self-exchange rates for the interconversion between NiML and (η^2-H_2)NiML. Exchange rates were determined *via* least-squares fitting of the VT ^{31}P NMR spectra using a two-site, non-mutual exchange model (see Experimental section and ESI† for details).[49,50] Good agreement was generally achieved between the experimental and simulated spectra, as illustrated in Fig. 3a for the VT ^{31}P NMR study of **1** under 1 atm H_2. Similar lineshape analyses were performed for each NiML complex, which allowed exchange rates to be determined at seven or more different temperatures between 213 K and 344 K (Fig. S42–S44†). Notably, the exchange rate decreases by a factor of ~6 at 298 K upon varying the supporting metal from Al to In (Table 4). Exchange rates at 298 K were found to correlate strongly with both H_2 binding free energies ($R^2 = 0.996$, Fig. S47†) and H–H bond distances in (η^2-H_2)NiML complexes ($R^2 = 0.958$, Fig. S48†), with slower kinetic rates of H_2 exchange for more thermodynamically favorable binding equilibria where H_2 is more activated. The H_2 binding equilibrium for complex **1** is especially dynamic, with interconversion between **1** and **1**-H_2 occurring over 28 000 times per second at 298 K and 1 atm H_2 (Fig. 3a and Table 4).

We propose a self-exchange mechanism comprised of H_2 loss from (η^2-H_2)NiML to generate NiML and free H_2, and H_2 binding to another NiML complex to form (η^2-H_2)NiML (Fig. 3c). The rate constants for H_2 loss from (η^2-H_2)NiML, k_{loss}, were determined at each T based on the exchange rates and the known equilibrium concentrations of (η^2-H_2)NiML (see ESI†). Eyring analyses for k_{loss} allowed for the determination of activation barriers for H_2 loss from (η^2-H_2)NiML complexes, as shown in Fig. 3b for **1**-H_2. Eyring plots for H_2 loss from **2**-H_2 and **3**-H_2 are shown in Fig. S49 and S50,† respectively. The free energy barriers for H_2 loss ($\Delta G^{\ddagger}_{loss}$) were found to be similar for all complexes (9.1 to 9.4 kcal mol^{-1}), with $\Delta H^{\ddagger}$ and $\Delta S^{\ddagger}$ values ranging from 9.3 to 11.3 kcal mol^{-1} and from −0.3 to +7.5 cal (mol K)$^{-1}$, respectively (Table 4). The fact that $\Delta S^{\ddagger}_{loss}$ values are positive or close to zero in all cases is consistent with the expected gain in H_2 freedom of motion, while positive $\Delta H^{\ddagger}_{loss}$ values suggest that partial Ni–H_2 bond breaking is the dominant process involved in reaching the transition state for H_2 loss. Interestingly, both $\Delta H^{\ddagger}_{loss}$ and $\Delta S^{\ddagger}_{loss}$ values for the (η^2-H_2)NiML complexes decrease as the supporting metal is varied down group 13 (Al > Ga > In; Table 4).

Fig. 3 (a) Selected VT ^{31}P NMR spectra of **1** under 1 atm H_2 from 215 to 298 K (red lines, toluene-d_8, 162 MHz) and corresponding simulated spectra (black lines), which were utilized to extract exchange rates at each T (standard deviations in parentheses). (b) Eyring plot of $\ln(k_{loss}/T)$ vs. $1/T$, where k_{loss} is the first-order rate constant for H_2 loss from **1**-H_2. (c) Proposed reaction coordinate diagram for chemical exchange between $(\eta^2$-$H_2)$NiML and NiML via unimolecular H_2 loss.

Table 4 Comparison of thermodynamic and kinetic binding parameters for H_2 self-exchange, binding, and loss for NiML complexes (**1**–**3**)[a]

Complex		**1**	**2**	**3**
Self-exchange[b]	Rate$_{ex}$ ($\times 10^4$)	2.82(3)	2.2(2)	0.437(5)
	Rate$_{rel}$	6.4	4.9	1.0
H_2 loss[c]	k_{loss} ($\times 10^6$)	55(3)	6.5(5)	0.60(3)
	$\Delta H^\ddagger_{loss}$	11.3(2)	10.1(4)	9.3(4)
	$\Delta S^\ddagger_{loss}$	7.5(1)	3.5(1)	−0.3(1)
	$\Delta G^\ddagger_{loss}$	9.1(2)	9.1(4)	9.4(4)
H_2 binding	$\Delta G^\circ_{1\,M}$[d]	−1.9(2)	−2.9(2)	−6.5(7)
	$\Delta G^\ddagger_{bind}$	7.2(3)	6.2(5)	2.9(8)

[a] All values determined for a standard state of 1 M H_2, 1 M for all other species in toluene-d_8, and 298 K. $\Delta G^\circ_{1\,M}$, $\Delta G^\ddagger$, and $\Delta H^\ddagger$ values are in units of kcal mol^{-1}, and $\Delta S^\ddagger$ values are in units of cal (mol K)$^{-1}$. Rate$_{ex}$ and k_{loss} are in s^{-1}, and rate$_{rel}$ is the relative rate. [b] [Ni]$_{total}$ = 7.5 mM. [c] $\Delta G^\ddagger_{loss} \approx \Delta G^\ddagger_{exchange}$ for unimolecular H_2 loss. [d] $\Delta G^\circ_{1\,M}$ are directly derived from values in Table 2 by converting the standard state for H_2 from 1 atm H_2 to 1 M. See ESI for details.

Furthermore, $\Delta S^\ddagger_{loss}$ values ($\sim$0 or >0) are consistent with unimolecular H_2 loss from $(\eta^2$-$H_2)$NiML, as opposed to H_2 self-exchange via an intermolecular LMNi$\cdots$H$_2$$\cdots$NiML transition state. Such a transition state also seems unlikely because of the steric clash between the diisopropyl ligand groups surrounding each Ni site. Using the proposed reaction coordinate diagram, one can further extract the free energy barrier for H_2 binding ($\Delta G^\ddagger_{bind}$) by using the thermodynamic relationship: $\Delta G^\ddagger_{loss} = \Delta G^\ddagger_{bind} - \Delta G^\circ_{1\,M}$. Of note, $\Delta G^\circ_{1\,M}$ is the free energy of H_2 binding after converting the H_2 standard state from 1 atm (as given in Table 2) to 1 M. Hence, the $\Delta G^\ddagger_{bind}$ values for **1**, **2**, and **3** are 7.2(3), 6.2(5), and $\sim$2.9(8) kcal mol^{-1}, respectively, where the activation barriers for H_2 binding are lower for more thermodynamically favorable binding equilibria (Table 4).

Activation barriers and rate constants for H_2 binding and loss have seldom been reported despite their relevance for many catalytic processes. $\Delta H^\ddagger_{loss}$ values for $(\eta^2$-$H_2)$NiML (9.3 to 11.3 kcal mol^{-1}) are comparable to those reported (in kcal mol^{-1}) for $[Ru(\eta^2$-$H_2)H_3(PPh_3)_3]^+$ (8.8),[31] $Cr(\eta^2$-$H_2)(CO)_3(PCy_3)_2$ (12.1),[10] $Ir(\eta^2$-$H_2)(H)_2X(P^tBu_2Me)_2$ (9.4 to 11.3 for X = Cl, Br, I),[40] and $Ir(\eta^2$-$H_2)(H)_2X(P^iPr_3)_2$ (10.1 to 11.4 for X = Cl, Br, I),[51] and are significantly lower than those reported for $W(\eta^2$-$H_2)(CO)_3(PCy_3)_2$ (16.9)[44] and $Ru(\eta^2$-$H_2)(H)_2(PPh_3)_3$ (17.9).[31] Perhaps the most thoroughly studied H_2 binding equilibrium is that of $W(\eta^2$-$H_2)(CO)_3(PCy_3)_2$, for which rate constants for both H_2 binding (k_{bind}) and loss (k_{loss}) have been directly measured to be $\sim$2 $\times$ 10^6 M^{-1} s^{-1} and 469 s^{-1} at 298 K, respectively.[44,52] In comparison, the k_{loss} values for $(\eta^2$-$H_2)$NiML complexes are 3 to 5 orders of magnitude greater than that for $W(\eta^2$-$H_2)(CO)_3(PCy_3)_2$ (Table 4). This can be rationalized by the fact that H_2 is much more activated in $W(\eta^2$-$H_2)(CO)_3(PCy_3)_2$, which co-exists with its dihydride species at 298 K ($K \sim$0.25).[7,44,45] In contrast, HNi(μ-H)ML dihydride species, which have some precedent in the literature,[24,53,54] have not been observed.[16,55] DFT calculations predict such a species to be unstable relative to $(\eta^2$-$H_2)$NiML by 12 to 19 kcal mol^{-1} under 1 atm H_2 (Table S25, S26 and Fig. S55†).

Part IV. Insights from quantum chemical calculations and UV-Vis spectra

Complexes **1**–**3** and NiLH$_3$ (**4**), as well as their H_2 and N_2 adducts, were investigated by density functional theory (DFT) calculations using several different functionals and basis sets (see Experimental section and Table S3†). The M06-D3 [56,57]/bs4 method gave the best agreement between the optimized and experimental geometries for the three Ni–In complexes: **3**, **3**-N_2, and **3**-H_2 (Tables S13–S15†).[16] On the other hand, the relative free energies (ΔG°) for H_2 and N_2 binding to **1**–**3** were best matched by M06-L[38]/bs1 (Tables S16 and S17†), which correctly predicted the trends of stronger H_2 binding than N_2 and increasing binding favorability for M = In > Ga > Al (Tables 2 and 3).

To better understand chemical bonding between H_2 and Ni in the $(\eta^2\text{-}H_2)$NiML complexes, we conducted energy decomposition analysis (EDA).[58] EDA allows for the total interaction energy (ΔE_{int}) between the H_2 and NiML fragments to be partitioned into the following terms: electrostatic energy (ΔE_{elstat}), Pauli repulsive interaction (ΔE_{Pauli}), dispersion (ΔE_{disp}), and covalent interaction (ΔE_{orb}).[58] The ΔE_{orb} term can be further divided into individual energy contributions associated with specific orbital interactions, and thereby allows for differentiation of σ, π, and δ bonding interactions. The extended transition-state method coupled with natural orbitals for chemical valence theory (ETS-NOCV[59]) was then utilized to analyze the bonding interactions between Ni and H_2. Fig. 4 illustrates the two most important NOCV pairs for the Ni–H_2 interaction in 3-H_2, in which chemical bonding is indicated by deformation in the electron densities ($\Delta\rho$). Overall, two orbital interactions are important: (1) σ-donation from the H_2 σ-bond to the empty Ni $4p_z$ orbital, which accounts for 56% of ΔE_{orb} and is comprised of $\Delta\rho_1$ (38%; Fig. 4) and $\Delta\rho_3$ (18%; Fig. S53†); and (2) π-back-donation from a Ni $3d_\pi$ orbital to the empty H_2 σ^* orbital, which accounts for 35% of ΔE_{orb}. Similarly, greater contributions of σ-donation (57–59% of ΔE_{orb}) compared to π-back-donation (34–35% of ΔE_{orb}) were also observed for Ni–H_2 orbital interactions in 1-H_2 and 2-H_2 (Table S22†).

The total interaction energy (ΔE_{int}) between the H_2 and Ni fragments becomes increasingly favorable in the order, $(\eta^2\text{-}H_2)$NiLH$_3$ < 1-H_2 < 2-H_2 < 3-H_2 (Table S21†). Of interest, the less favorable ΔE_{int} predicted for $(\eta^2\text{-}H_2)$NiLH$_3$ arises from a large, unfavorable ΔE_{Pauli} term, which is the repulsive interaction energy between like spins in the H_2 and NiLH$_3$ fragments. This makes sense as NiLH$_3$ lacks a Ni→M interaction that would result in attenuation of Ni electron density. Within the $(\eta^2\text{-}H_2)$NiML series, both the ΔE_{elstat} and ΔE_{orb} terms become more favorable as M is varied down the group 13 triad (Table S21†). Furthermore, the greater relative importance of σ-donation to H_2 binding than π-back-donation is consistent with the trend that H_2 binding favorability increases as the Ni center becomes more electron-deficient, as judged by the Ni(I/0) redox potentials (Fig. S71 and Table S39†).[16] Hence, we propose that increased electron-withdrawal via Ni→M dative bonding as M is varied down group 13 induces stronger electrostatic and covalent interactions between H_2 and NiML, with a concomitant decrease in unfavorable Pauli repulsion between the two fragments.

Given the rarity of H_2 and N_2 binding to a Ni(0) metal center, we next sought to understand the specific electronic perturbations of the supporting group 13 metal ion that poise NiML to bind small molecules. To lend insight, UV-Vis spectroscopy studies in conjunction with time-dependent density functional theory (TD-DFT) calculations were conducted to investigate the electronic structure of complexes 1–4 and their H_2 and N_2 adducts. The UV-Vis spectra of NiLH$_3$ and 1–3 are shown in Fig. 5a (THF, 298 K), along with the corresponding TD-DFT predicted spectra, where M06-D3/bs4 showed the best agreement with experiment (Fig. 5b and Table S29†). We also sought to understand how the binding of H_2 and N_2 to the NiML complexes further impacts electronic structure. In this regard, it is notable that small-molecule binding to NiML often manifests in vibrant color changes. For example, exposure of a THF solution of 3 under Ar to an N_2 or H_2 atmosphere resulted in a color change from a deep red-purple color to a lighter red (3-N_2) or yellow-brown (3-H_2), respectively (Fig. 5c).

The UV-Vis spectra of 1–3 share the same pattern of three peaks between 400 and 800 nm, which are marked with asterisks in Fig. 5a and listed in Table 5 as peaks I, II, and III. These peaks all red-shift upon varying the supporting metal from Al to Ga to In. The TD-DFT calculated transition energies for 1–3 agree reasonably well with experiment, with the predicted excitations generally blue-shifted by 0.04 to 0.3 eV for peaks I to III (Table 5). The TD-DFT results also correctly predicted the red-shift of all peaks for 2 relative to 1, but the subtle spectral differences between 2 and 3 were not discerned by TD-DFT despite testing several methods (Table S29, Fig. S57 and S58†). For NiLH$_3$, a broad absorption feature is observed at ~500 nm, which was fit with two overlapping peaks with maxima at 491 and 533 nm, along with a low-intensity shoulder at 663 nm (Table S27, Fig. S56†).

UV-Vis peaks I–III for NiLH$_3$ and 1–3 were assigned based on the TD-DFT results (Table 5). Each peak corresponds to an electronic excitation from either a Ni 3d orbital or a ligand-based molecular orbital (MO) to the lowest unoccupied molecular orbital (LUMO), the latter of which is highly similar for all complexes. For NiLH$_3$, the LUMO has both Ni $4p_z$ and P 4p character, whereas the LUMO for complexes 1–3 also has additional contributions from Ni (3d, 4s) and M (s, p_z) atomic orbitals (Fig. S59 and Table S31†). For all complexes, peaks I and II arise from electronic excitations to the LUMO from the Ni d_{xy}/$d_{x^2-y^2}$ and d_{xz}/d_{yz} orbitals, respectively. Peak III for NiLH$_3$ is a transition from a pure d_{z^2} orbital to the LUMO, while peak III for 1–3 is a more complex transition from a mixed ligand-based arene π^* MO with partial Ni d_{z^2} character to the LUMO (Table S28†).

Based on these transition assignments, semi-quantitative MO diagrams for NiLH$_3$ and 1–3 can be constructed (Fig. 6).

Fig. 4 The two dominant NOCV pairs in 3-H_2 and their associated deformation densities ($\Delta\rho_1$, top right; $\Delta\rho_2$, bottom right; contour isovalue = 0.04 a.u.). The colors of the deformation densities indicate the flow of electrons, from red to blue, involved in the Ni–H_2 interaction.

Fig. 5 (a) UV-Vis spectra of NiLH₃ (grey), 1 (red), 2 (blue), and 3 (black) obtained in THF at room temperature. Inset is a close-up of the 600–800 nm range. (b) TD-DFT predicted spectra of NiLH₃ and 1–3 (M06-D3/bs4, SMD/THF) shown as dotted lines. (c) UV-Vis spectra of 3 (under Ar, black), 3-N₂ (under 1 atm N₂, pink), and 3-H₂ (under 1 atm H₂, cyan) in THF at 298 K, with TD-DFT plots shown in the inset. Note that small features corresponding to 3 can be seen in the UV-Vis spectrum of 3-N₂ due to the equilibrium binding of N₂ under these conditions. Asterisks in spectra correspond to bands I, II, or III, as listed in Table 5.

Table 5 UV-Vis peaks (nm) for NiLH₃ and 1–3, with TD-DFT data (in parentheses) and transition assignments

Peak	Transition	NiLH₃	1	2	3
I	$d_{xy}/d_{x^2-y^2} \to$ LUMO	663 (490)	600 (573)	638 (650)	699 (642)
II	$d_{yz}/d_{xz} \to$ LUMO	491 (413)	490 (437)	508 (478)	530 (475)
III	π-ligand + $d_{z^2} \to$ LUMO	533 (443)[a]	430 (410)	464 (448)	488 (449)

[a] Pure Ni $d_{z^2} \to$ LUMO transition.

For NiLH₃, the d-orbital manifold is consistent with that expected for a trigonal-planar metal center with three σ-donors: the degenerate $d_{xy}/d_{x^2-y^2}$ orbitals are the most destabilized, followed by d_{z^2}, and then the d_{xz}/d_{yz} set. For 1–3, the presence of the supporting group 13 metal ion results in the stabilization of the Ni 3d$_{z^2}$ orbital via Ni→M(p$_z$/s) dative bonding, which is consistent with the blue shift in the predicted pure 3d$_{z^2}$ → LUMO transitions in the bimetallic NiML complexes (363 to 385 nm; Table S30†) relative to NiLH₃ (443 nm). The Ni d_{xz}/d_{yz} orbitals, on the other hand, are destabilized upon the introduction of the supporting metal and its variation down group 13. Presumably, the π-back-bonding interaction, Ni d_{xz}/d_{yz} → P–C σ*, becomes weaker as the Ni center becomes more electron-deficient due to stronger electron withdrawal by the supporting metal (In > Ga > Al > no support).[16] In support, both the Ni–P bonds elongate and the ³¹P NMR signal shifts downfield from NiLH₃ to 1 to 2 to 3.

Another notable MO trend involves the energy difference between the Ni d_{xz}/d_{yz} orbitals and the LUMO, as reflected in the peak II energies, which decrease upon the introduction and variation of the supporting metal down group 13. This particular energy gap is important because the LUMO and the Ni d_{xz}/d_{yz} orbitals are the frontier Ni-based MOs that participate in small-molecule binding, with the Ni-based LUMO accepting σ-donation from either the H₂ σ-bond or the N₂ lone pair, and the Ni d_{xz}/d_{yz} orbitals participating in π-back-bonding to either the H₂ σ* or N₂ π* LUMOs. Overall, the Ni d_{xz}/d_{yz} → LUMO excitation energy decreases by ~0.2 eV across the NiML complexes, from 2.53 eV in 1 to 2.44 eV in 2 to 2.34 eV in 3 (Table S28†). Thus, it is reasonable to propose that varying the supporting metal from Al to Ga to In results in the destabilization of the Ni d_{xz}/d_{yz} orbital set and the stabilization of the Ni-based LUMO, such that both become more energetically accessible to interact with small-molecule substrates.

The involvement of the LUMO in small-molecule binding is further supported by examining the changes in the UV-Vis spectra for 3 upon binding H₂ and N₂ (Fig. 5c). Notably, both the experimental and theoretical spectra of 3-H₂ and 3-N₂ lack any intense features between 400 and 700 nm. Instead, the lowest energy transitions for 3-H₂ and 3-N₂ are predicted at 375 and 391 nm, respectively. The shift to higher energy excitations for the H₂ and N₂ adducts can be qualitatively explained by the nature of their acceptor MOs, which we define as the lowest-energy unoccupied MO with significant Ni character, rather

Fig. 6 (Top) MO diagrams of NiLH$_3$ and complexes **1–3**. The ligand field energies (in eV) are based on UV-Vis data (Table 5). TD-DFT calculated energies are shown (in eV, italicized within parentheses) when experimental values were not obtainable. (Bottom) MOs for complex **2**, which are representative of those for the series. Note that MO energies are drawn to scale, but energy comparisons across the complexes are qualitative.

than those that are ligand based (Fig. S60–S63 and Tables S33–S38†). For both **3**-H$_2$ and **3**-N$_2$, the acceptor MO appears to be an anti-bonding combination of the LUMO in **3** and the donor MO of the small molecule (Fig. S64†). Thus, upon small-molecule binding *via* the dominant σ-donation interaction with the LUMO of NiML, the resulting acceptor orbitals in (L′)NiML adducts (L′ = H$_2$, N$_2$) to which electrons can be excited are of higher energy relative to the Ni 3d manifold, and thereby give rise to higher energy electronic transitions.

Part V. Linear free-energy relationships

We examined linear free-energy relationships across the NiML series to quantify the effect of the supporting group 13 metal on the thermodynamics and kinetics of small-molecule binding. For H$_2$ binding, an excellent correlation was observed between the thermodynamic free energies ($\Delta G^{\circ}_{1\,M}$) and the free energies

of activation ($\Delta G^{\ddagger}_{bind}$), where more exergonic binding equilibria have smaller activation barriers ($R^2 = 0.999$, Fig. 7a). The slope of +0.93 in the $\Delta G^{\ddagger}_{bind}$ *versus* $\Delta G^{\circ}_{1\,M}$ plot indicates that a decrease of ~1 kcal mol^{-1} in $\Delta G^{\circ}_{1\,M}$ for H$_2$ binding corresponds to a commensurate lowering of the free energy barrier. Reasonably strong correlations were also found between the Ni 3d$_{xz}$/d$_{yz}$ → LUMO excitation energy and ΔG° for H$_2$ ($R^2 = 0.924$) and N$_2$ ($R^2 = 0.963$) binding (Fig. 7b). This correlation makes sense since the Ni 3d$_{xz}$/d$_{yz}$ orbitals and the LUMO are the Ni-based frontier orbitals that participate in small-molecule binding (*vide supra*). The slopes of the plots of ΔG° for H$_2$ and N$_2$ binding *versus* the Ni 3d$_{xz}$/d$_{yz}$ → LUMO excitation energy (in kcal mol^{-1}) are close to unity, where a decrease of 1 kcal mol^{-1} in the Ni 3d$_{xz}$/d$_{yz}$ → LUMO excitation energy is associated with a nearly equivalent increase in the favorability of H$_2$/N$_2$ binding.

The isostructural nature of the (η^2-H$_2$)NiML series allows us to further interrogate which intrinsic properties of the group 13
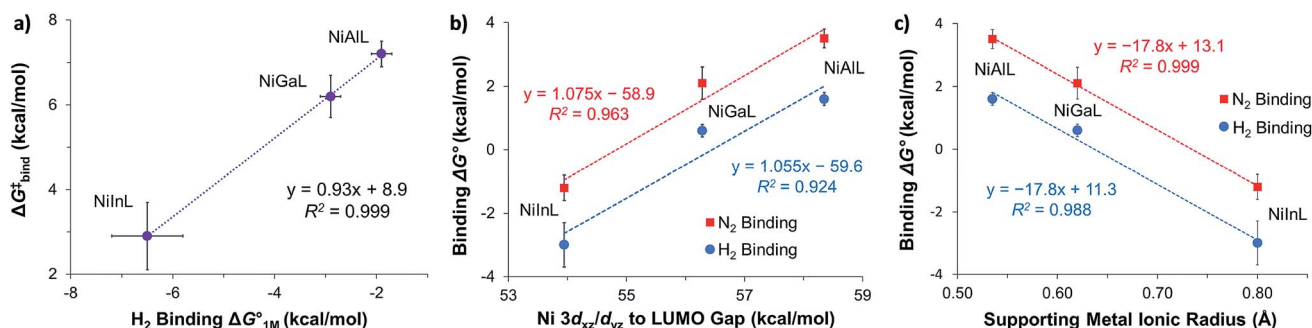

Fig. 7 (a) Plot of free energy barrier for H$_2$ binding ($\Delta G^{\ddagger}_{bind}$) *vs.* thermodynamic free energy for H$_2$ binding ($\Delta G^{\circ}_{1\,M}$), with the standard deviation in all values shown by error bars and all standard states defined to be [H$_2$] = 1 M in toluene-d$_8$. (b–c) Plots of ΔG° for H$_2$ (blue circles) and N$_2$ binding (red squares) *vs.* Ni 3d$_{xz}$/d$_{yz}$ to LUMO energy gap (b) and *vs.* supporting metal Shannon ionic radii (c). Ni 3d$_{xz}$/d$_{yz}$ to LUMO energy gaps were measured experimentally by UV-Vis spectroscopy with transition assignments from TD-DFT calculations (see ESI† and Table 5).

support (M) dictate the favorability of H_2 and N_2 binding. A strong negative correlation was found between the size of the supporting metal, as represented by Shannon's M(III) ionic radii,[60] and $\Delta G°$ for both H_2 ($R^2 = 0.988$) and N_2 ($R^2 = 0.999$) binding (Fig. 7c), where larger supporting ions induce more exergonic binding. The finding that larger supporting metals better poise Ni for small-molecule binding is likely a composite effect of both electronic and steric factors. Larger group 13 supporting metals show stronger Ni→M bonding interactions (Table S24b†) and shift the Ni(0/I) oxidation to more positive potentials,[16] both of which should lower the Pauli repulsion associated with binding a donor (Fig. S71†). Also, larger group 13 ions force Ni to move further above the P_3-plane which should minimize the structural reorganization energy associated with small-molecule binding (Fig. S72†).

The confluence of steric and electronic effects is also supported by the fact that neither effect can solely account for the observed trends. For example, the position of Ni above the P_3-plane is identical for both Al and Ga (0.13 Å), despite their distinct differences in $\Delta G°$ for H_2/N_2 binding. Also, correlations between $\Delta G°$ for H_2/N_2 binding and Ni redox potentials are comparatively poor, whether one considers the Ni(0/I) oxidation or the Ni(−I/0) reduction potentials ($R^2 = 0.726$ to 0.891, Fig. S68 and S69†).[16,61] Typically Lewis acidity is expected to correlate with σ-accepting ability, yet no linear relationship exists between $\Delta G°$ for H_2/N_2 binding and the relative Lewis acidities of group 13 metals, as given by the pK_a values of the corresponding $M(H_2O)_6^{3+}$ complexes ($R^2 = 0.02–0.05$, Fig. S66†).[62,63] It is plausible that the Lewis acidity scale based on M–OH_2 bonds, where H_2O is the Lewis base, is an inappropriate benchmark for a Ni(0) Lewis base. You and Gabbaï have recently proposed that the double-decker ligand framework, which imposes spatial constraints, may "accentuate" the influence of the group 13 ion's size.[64] It is noteworthy that $\Delta G°$ values for H_2 ($R^2 = 0.945$) and N_2 ($R^2 = 0.977$) binding correlate reasonably well with the degree of Ni→M dative bonding, as quantified by the ratio of the solid-state Ni–M bond distance to the sum of the covalent radii of Ni and M (Fig. S67†).[65,66] This finding is consistent with the hypothesis that group 13 metals can significantly tune the reactivity of a proximal Ni center via a direct Ni(0)→M(III) dative interaction.

Conclusion

H_2 and N_2 binding is atypical for Ni complexes and facilitating H_2 activation to form reactive Ni(η^2-H_2) and/or Ni–H species poses a difficult hurdle for developing homogeneous Ni catalysts for H_2 oxidation, proton reduction, and related processes. Excitingly, we find that supporting Ni with group 13 metals induces the binding of H_2 and N_2 to Ni, with H_2 binding found to be ~2 kcal mol^{-1} more favorable than N_2 binding in each case. The pivotal role of the supporting metal in promoting binding to the NiML complexes is highlighted by the inability of NiLH$_3$, a similarly ligated mononuclear Ni center, to bind H_2 or N_2 under any conditions examined. The dramatic tuning effect of the supporting group 13 metal is illustrated by the wide range of $\Delta G°$ values for H_2 binding, which span ~8 kcal mol^{-1}

(including NiLH$_3$) and nearly cover the entire range of previously reported values. H_2 binding to NiInL (3) is more exergonic than any such equilibrium reported, allowing for solid-state characterization of (η^2-H_2)NiInL (3-H_2) via neutron diffraction, which is unprecedented for an H_2 adduct of Ni or any d^{10} metal.

Theoretical calculations have provided important insights into the role of the supporting metal in promoting small-molecule binding. Specifically, complementary σ-interactions are proposed based on ETS-NOCV calculations, where H_2 → Ni σ-donation to the energetically-accessible Ni(4p$_z$)-based LUMO is the dominant binding interaction, which is likely induced by electron withdrawal from Ni via the dative Ni(0)→M(III) bond. The involvement of the LUMO in small-molecule binding is supported by TD-DFT and UV-Vis studies, along with the strong correlation between $\Delta G°$ values for H_2/N_2 binding and the Ni 3d$_{xz}$/d$_{yz}$ → LUMO excitation energy. Notably, the size of the supporting M(III) ion correlates best with $\Delta G°$ values for H_2 and N_2 binding, with larger group 13 supporting metals inducing more favorable binding by: rendering Ni more electron-deficient, favoring stronger Ni→M interaction, and minimizing the structural reorganization energy. Moreover, thermodynamically favorable H_2 binding equilibria (In > Ga > Al) have proportionally smaller free energies of activation.

Overall, a thorough understanding of H_2 and N_2 binding to NiML complexes, and the integral role of the supporting metal therein, has been presented. Future work will explore the impact of the thermodynamics and kinetics of H_2 binding equilibria on catalytic CO_2 hydrogenation reactivity, where H_2 binding to displace formate has been found to be the rate-determining step in catalysis.[20,67] Additionally, the generalizability of the strategy of favorably altering base-metal reactivity via interactions with group 13 supporting metals will be assessed, and efforts are currently underway to extend our studies to other ligand frameworks and transition metals.

Experimental section

Additional information is provided in the ESI.†

General considerations

Unless otherwise stated, all manipulations were performed under an Ar or N_2 atmosphere inside a glovebox or using standard Schlenk techniques. Standard solvents were deoxygenated by sparging with N_2 and dried by passing through activated alumina columns of a SG water solvent purification system. Deuterated solvents and HD gas (97% D content) were purchased from Cambridge Isotope Laboratories, Inc. Deuterated solvents were degassed via freeze–pump–thaw cycles, and either stored over activated 4 Å molecular sieves or stirred with Na–K alloy and distilled. N_2 and H_2 gases were purchased from Matheson Trigas, Inc., and a gas mixture of 10% H_2/90% Ar was purchased from Praxair, Inc. All other reagents were purchased from commercial vendors and used without purification unless otherwise noted. The ligand N(o-(NHCH$_2$P^{i}Pr$_2$)C$_6$H$_4$)$_3$ (abbreviated as LH$_3$), NiAlL (1), NiGaL (2), NiInL (3), (η^2-H_2)NiGaL (2-H_2), (N_2)NiInL (3-N_2), (η^2-H_2)NiInL (3-H_2), and NiLH$_3$ (4) were

synthesized according to the literature.[16,34,68] ^{1}H and ^{31}P NMR spectra were recorded on Bruker (400 or 500 MHz) or Varian (500 MHz) spectrometers and referenced to internal residual solvent (or H_3PO_4 for ^{31}P NMR spectra). For VT NMR experiments, the temperature was calibrated using a methanol (≤ 298 K) or an ethylene glycol (>298 K) standard. UV-Vis spectra were collected on a Cary-14 instrument. Cyclic voltammetry experiments were performed using a CHI Instruments 620D potentiostat. The one-cell setup utilized a glassy carbon working electrode, platinum wire counter electrode, and $Ag/AgNO_3$ reference electrode in CH_3CN.

In situ generation of (η^2-H_2)NiAlL (abbreviated as 1-H_2)

A solution of **1** (15 mg, 19.6 μmol) in THF-d_8 (~0.30 mL) was added to a PEEK NMR cell and pressurized to 34 atm H_2. The following NMR data are reported at 34 atm H_2; an equilibrium between **1** and **1**-H_2 can also be observed under 1 atm H_2 at low T. ^{1}H{^{31}P} NMR (ppm, THF-d_8, 232 K, 500 MHz): 7.34 (br, 3H, ArH), 6.87 (br, 3H, ArH), 6.34 (br, 6H, ArH), 3.00 (br, 3H, C*H*H′), 2.87 (br, 3H, CH*H*′), 2.10 (m, 6H, C*H*(CH$_3$)$_2$), 1.27 to 0.90 (36H, CH(C*H*$_3$)$_2$), −1.5 (br, 2H, (H_2)Ni, T_1 (min) $\leq 0.49(5)$ s at 200 K). ^{31}P NMR (ppm, 200 K, 202.4 MHz): 44.9 (in THF-d_8), or ~44.3 (in toluene-d_8). The lability of H_2 precluded elemental analysis from being obtained.

In situ observation of (N_2)NiAlL (1-N_2) and (N_2)NiGaL (2-N_2)

A solution of **1** (3.7 mg, 4.8 μmol) in toluene-d_8 (0.30 mL) was added to a PEEK NMR cell and pressurized to 51 atm N_2. Similarly, a solution of **2** (5.0 mg, 6.2 μmol) in toluene-d_8 (0.41 mL) was added to a J. Young NMR tube under 1 atm N_2. Neither **1**-N_2 nor **2**-N_2 was isolable due to lability of the N_2 ligand. Both **1**-N_2 and **2**-N_2 were observed in the presence of **1** and **2**, respectively, which limited ^{1}H NMR characterization due to overlapping resonances. For **1**-N_2: ^{31}P NMR (ppm, toluene-d_8, 190 K, 51 atm N_2, 202.4 MHz): ~32.2. For **2**-N_2: ^{31}P NMR (ppm, toluene-d_8, 193 K, 1 atm N_2, 162 MHz): ~43.5.

X-ray and neutron diffraction crystallographic and structure refinement details

X-ray diffraction. A gold block of (η^2-H_2)NiInL (3-H_2) was placed onto the tip of a MiTeGen Dual-Thickness Micro-Loop™ and mounted on a Bruker Photon II CMOS diffractometer for data collection at 100(2) K (Table 6). The data collections were carried out using Mo Kα radiation (graphite monochromator), and the data intensity was corrected for absorption and decay (SADABS).[69] Final cell constants were obtained from least-squares fits of all measured reflections. The structure was solved using SHELXT-16 and refined using SHELXL-16, which were executed from the ShelXle graphical user interface.[70] A direct-methods solution was calculated which provided most non-hydrogen atoms from the E-map. Full-matrix least-squares/difference Fourier cycles were performed to locate the remaining non-hydrogen atoms. All non-hydrogen atoms were refined with anisotropic displacement parameters. Hydrogen atoms were placed in ideal positions and refined as riding atoms with relative isotropic

Table 6 Crystallographic details for **3**-H_2 (X-ray and neutron structures)

Radiation type	X-ray	Neutron
Chemical formula	$C_{39}H_{62}N_4P_3InNi$	$C_{39}H_{62}N_4P_3InNi$
F_w	853.36	853.36
Cryst syst	Orthorhombic	Orthorhombic
Space group	$P2_12_12_1$	$P2_12_12_1$
a (Å)	12.2127(4)	12.2010(10)
b (Å)	14.5402(5)	14.5638(12)
c (Å)	22.5601(8)	22.547(2)
α (deg)	90	90
β (deg)	90	90
γ (deg)	90	90
V (Å^3)	4006.1(2)	4006.4(6)
Z	4	4
λ (Å), μ (mm^{-1})	0.71073, 1.198	0.60–3.36, 0.1570 + 0.1306λ
T (K)	100(2)	100(2)
Θ	2.285 to 36.348	7.352 to 78.740
Reflns collected	237 431	14 303
Unique reflns	19 473	4718
Data/restraint/parameters	19 473/0/451	4718/1068/991
R1, wR2 ($I > 2\sigma(I)$)	0.0181, 0.0392	0.0620, 0.1262

displacement parameters,[71] with the exception of the apical H_2 ligand in **3**-H_2, for which the H atoms were sufficiently resolved in the Fourier difference map to allow tentative placement. Images were rendered using POV-ray.[72]

Neutron diffraction. Neutron diffraction data were collected using the TOPAZ single-crystal time-of-flight (TOF) Laue diffractometer at the Spallation Neutron Source (SNS), at Oak Ridge National Laboratory (Oak Ridge, TN).[73] A block-shaped crystal of **3**-H_2, with dimensions of 0.35 × 0.30 × 0.30 mm, was grown from a concentrated toluene solution under 1 atm H_2 at ~280 K for several weeks. The crystal was mounted on the tip of a polyimide capillary using fluorinated grease and transferred to the TOPAZ goniometer for data collection at 100 K (Table 6). To ensure good coverage and redundancy, data were collected using crystal orientations optimized with CrystalPlan software[74] for optimal coverage of symmetry-equivalent reflections of the orthorhombic cell. The integrated raw Bragg intensities were obtained using the 3-D ellipsoidal Q-space integration in accordance with previously reported methods.[75] Data reduction, including neutron TOF spectrum, Lorentz, and detector efficiency corrections, was carried out with the ANVRED3 program.[76] A spherical absorption correction was applied with $\mu = 0.1570 + 0.1306 \lambda$ cm^{-1}. The reduced data were saved as SHELX HKLF2 format, in which the wavelength is recorded separately for each reflection, and data were not merged. Starting with the X-ray structure at 100 K as an input model (where all the H atoms were placed except for the H_2 ligand), the neutron crystal structure was refined using the SHELXL-14/7 program[70,71] with RIGU restraints for the H-atoms' anisotropic displacement parameters.[77]

General procedure for H_2/N_2 binding studies

A toluene-d_8 solution of NiML (15 mM) was filtered and transferred to either a J. Young NMR tube (≤ 3.8 atm) or a PEEK NMR

cell ($\geq$6.8 atm).[78,79] For high-pressure studies, the PEEK cell was sealed and connected to a high-pressure line equipped with a vacuum pump and an ISCO syringe pump. The line was purged with H_2 or N_2 gas three times. Next, the headspace was degassed by opening the PEEK cell to static vacuum (3 × 30 s), and H_2 or N_2 gas was then delivered to the cell from an ISCO syringe pump running constantly at the desired pressure (*i.e.* continuous gas feed). The contents of the PEEK cell were mixed using a vortex mixer for ~15 min prior to NMR data collection to allow for pressure stabilization and equilibration. For low-pressure studies, J. Young NMR tubes were pressurized after freeze–pump–thaw cycles. VT ^{31}P NMR spectra were acquired at several different T (193 to 368 K) in all studies, with an adequate number of scans collected (typically 64 to 160 scans) to quantify the observed peak position (for fast chemical exchange) and/or the relative peak integrations (for slow chemical exchange). ^{31}P spectra were typically collected with a recycle delay time of 2 s and an acquisition time of 1.68 s. In cases where quantitative integration of multiple peaks was desired, a longer delay time of 10 s was used.

CAUTION: H_2 is a highly flammable gas. Pressurized vessels must be handled with care using proper personal protective equipment. PEEK cells were employed for the high-pressure NMR studies, as described previously.[78,79]

General procedure for kinetic studies of H_2 self-exchange

A solution of NiML (7.5 mM in 0.70 mL) was prepared in toluene-d_8 and transferred to a J. Young NMR tube. VT ^{31}P NMR spectra were obtained at various T ($\geq$7 data points, 214 K to 344 K) for samples under 1 atm Ar to determine intrinsic linewidths and chemical shifts for NiML complexes. Subsequently, after freeze–pump–thaw cycles, the VT ^{31}P NMR profile was obtained under 1 atm H_2. NMR lineshape analysis was performed using the gNMR (version 5.0) program[80] to extract H_2 self-exchange rates at each T (see ESI for details†). ^{31}P NMR spectra were typically collected with a delay time of 2 s, an acquisition time of 1.68 s, and with 160 scans.

Computational methods

Density functional theory (DFT). DFT calculations were performed using the Gaussian 09 program package.[81] Four functionals (M06-L,[38] M06-D3,[56,57] PBE0,[82] and PBE0-D3 [56,82]) and five basis sets (denoted as bs0 to bs4, Table S3†) were evaluated. The M06-L/bs1 method (def2-TZVPP for H_2, N_2, Ni, Al, Ga, and In, with the SDD effective core potential[83] for In; def2-TZVP basis set for N, P; and def2-SVP for C and H atoms)[84] gave the best match to the experimental binding energies, and had been used in related prior studies.[67] Geometric structures were optimized in the gas phase at 0 K, using the crystal structure atomic coordinates as the initial geometries when available (**1–3**, **3**-H_2, and **3**-N_2). Vibrational frequency analyses were performed with the harmonic approximation to confirm the nature of all species (0 and 1 imaginary frequency for ground-state and transition-state structures, respectively). Unless otherwise noted, Gibbs free energies at 298.15 K and 1 atm were computed by adding zero-point vibrational energies and thermal corrections. Solvation effects

were considered by performing single-point calculations for all stationary points using the SMD solvation model.[85] The H_2 and N_2 binding energies for NiML were calculated according to the following equation:

$$X_{(g)} + NiML_{(solv)} \rightarrow X\text{-}NiML_{(solv)} \quad (3)$$

In eqn (3), $X_{(g)}$ is H_2 or N_2, and the standard state is defined as 1 atm for $X_{(g)}$. The overall energy for eqn (3) was determined based on the gas-phase free energies for H_2 or N_2 and the Gibbs free energies with solvation (in toluene) for $NiML_{(solv)}$ and $X\text{-}NiML_{(solv)}$.

Energy decomposition analysis (EDA). The EDA method[58] was implemented in the Amsterdam Density Functional (ADF 2016)[86,87] program package to study chemical bonding between H_2 and Ni in the (η^2-H_2)NiML complexes. Single-point energy calculations were performed using PBE0-D3/TZ2P[88] on the M06-L/bs1-optimized geometries. Relativistic effects for In were included by applying the zeroth-order regular approximation (ZORA).[89]

EDA breaks the total interaction energy (ΔE_{int}) between the H_2 and NiML fragments into four components, as shown in eqn (4):

$$\Delta E_{int} \text{(EDA)} = \Delta E_{elstat} + \Delta E_{Pauli} + \Delta E_{orb} + \Delta E_{disp} \quad (4)$$

ΔE_{elstat} is the attractive, quasi-classical electrostatic interaction between the electrons and the nuclei; ΔE_{Pauli} is the repulsive interaction between the occupied orbitals of the fragments; ΔE_{orb} is the interaction between the occupied molecular orbitals of one fragment and the unoccupied molecular orbitals of the other fragment; and, ΔE_{disp} corresponds to the dispersive effects between the two fragments. The extended transition state—natural orbitals for chemical valence (ETS-NOCV) method,[59] in combination with the energy decomposition scheme, was utilized to break down the orbital interaction component (ΔE_{orb}) into contributions from specific NOCV pairs (see ESI for further details†).

Time-dependent (TD) DFT calculations. TD-DFT calculations (M06-D3/bs4, Gaussian 09) with solvent considerations (SMD, THF) were performed to aid in assigning electronic transitions in the absorption spectra of $NiLH_3$ (**4**), NiML (**1–3**), (η^2-H_2) NiML, and (N_2)NiML complexes (M = Al, Ga, In). The basis sets denoted by bs4 were used: LANL2DZ[90] for In and 6-311G(d,p)[91] for all other atoms.

Conflicts of interest

The authors declare no competing financial interests.

Acknowledgements

References

1 L. Alig, M. Fritz and S. Schneider, *Chem. Rev.*, 2019, **119**, 2681–2751.

2 S. J. C. Robinson and D. M. Heinekey, *Chem. Commun.*, 2017, **53**, 669–676.

3 R. H. Morris, *Acc. Chem. Res.*, 2015, **48**, 1494–1502.

4 P. J. Chirik, *Acc. Chem. Res.*, 2015, **48**, 1687–1695.

5 R. M. Bullock and M. L. Helm, *Acc. Chem. Res.*, 2015, **48**, 2017–2026.

6 R. H. Crabtree, *Chem. Rev.*, 2016, **116**, 8750–8769.

7 G. J. Kubas, *Chem. Rev.*, 2007, **107**, 4152–4205.

8 P. G. Jessop and R. H. Morris, *Coord. Chem. Rev.*, 1992, **121**, 155–284.

9 G. J. Kubas, *Catal. Lett.*, 2005, **104**, 79–101.

10 J. M. Millar, R. V. Kastrup, M. T. Melchior, I. T. Horvath, C. D. Hoff and R. H. Crabtree, *J. Am. Chem. Soc.*, 1990, **112**, 9643–9645.

11 A. A. Gonzalez and C. D. Hoff, *Inorg. Chem.*, 1989, **28**, 4295–4297.

12 D. G. Abrecht and B. Fultz, *J. Phys. Chem. C*, 2012, **116**, 22245–22252.

13 D. E. Prokopchuk, G. M. Chambers, E. D. Walter, M. T. Mock and R. M. Bullock, *J. Am. Chem. Soc.*, 2019, **141**, 1871–1876.

14 D. L. M. Suess, C. Tsay and J. C. Peters, *J. Am. Chem. Soc.*, 2012, **134**, 14158–14164.

15 M. V. Vollmer, J. Xie and C. C. Lu, *J. Am. Chem. Soc.*, 2017, **139**, 6570–6573.

16 R. C. Cammarota and C. C. Lu, *J. Am. Chem. Soc.*, 2015, **137**, 12486–12489.

17 B. R. Barnett, C. E. Moore, P. Chandrasekaran, S. Sproules, A. L. Rheingold, S. DeBeer and J. S. Figueroa, *Chem. Sci.*, 2015, **6**, 7169–7178.

18 T.-P. Lin, C. R. Wade, L. M. Pérez and F. P. Gabbaï, *Angew. Chem., Int. Ed.*, 2010, **49**, 6357–6360.

19 T.-P. Lin, R. C. Nelson, T. Wu, J. T. Miller and F. P. Gabbaï, *Chem. Sci.*, 2012, **3**, 1128–1136.

20 R. C. Cammarota, M. V. Vollmer, J. Xie, J. Ye, J. C. Linehan, S. A. Burgess, A. M. Appel, L. Gagliardi and C. C. Lu, *J. Am. Chem. Soc.*, 2017, **139**, 14244–14250.

21 J. Takaya and N. Iwasawa, *J. Am. Chem. Soc.*, 2017, **139**, 6074–6077.

22 P. Steinhoff, M. Paul, J. P. Schroers and M. E. Tauchert, *Dalton Trans.*, 2019, **48**, 1017–1022.

23 B. A. Connor, J. Rittle, D. VanderVelde and J. C. Peters, *Organometallics*, 2016, **35**, 686–690.

24 W. H. Harman, T. P. Lin and J. C. Peters, *Angew. Chem., Int. Ed.*, 2014, **53**, 1081–1086.

25 R. H. Morris and R. J. Wittebort, *Magn. Reson. Chem.*, 1997, **35**, 243–250.

26 P. A. Maltby, M. Schlaf, M. Steinbeck, A. J. Lough, R. H. Morris, W. T. Klooster, T. F. Koetzle and R. C. Srivastava, *J. Am. Chem. Soc.*, 1996, **118**, 5396–5407.

27 G. J. Kubas, C. J. Burns, J. Eckert, S. W. Johnson, A. C. Larson, P. J. Vergamini, C. J. Unkefer, G. R. K. Khalsa, S. A. Jackson and O. Eisenstein, *J. Am. Chem. Soc.*, 1993, **115**, 569–581.

28 N. A. Eberhardt and H. Guan, *Chem. Rev.*, 2016, **116**, 8373–8426.

29 W. A. Gunderson, D. L. M. Suess, H. Fong, X. Wang, C. M. Hoffmann, G. E. Cutsail, J. C. Peters and B. M. Hoffman, *J. Am. Chem. Soc.*, 2014, **136**, 14998–15009.

30 R. S. Rowland and R. Taylor, *J. Phys. Chem.*, 1996, **100**, 7384–7391.

31 J. Halpern, L. Cai, P. J. Desrosiers and Z. Lin, *J. Chem. Soc., Dalton Trans.*, 1991, 717–723.

32 R. H. Crabtree and D. G. Hamilton, *J. Am. Chem. Soc.*, 1986, **108**, 3124–3125.

33 T. A. Luther and D. M. Heinekey, *Inorg. Chem.*, 1998, **37**, 127–132.

34 L. J. Clouston, R. B. Siedschlag, P. A. Rudd, N. Planas, S. Hu, A. D. Miller, L. Gagliardi and C. C. Lu, *J. Am. Chem. Soc.*, 2013, **135**, 13142–13148.

35 M. P. Williamson, *Prog. Nucl. Magn. Reson. Spectrosc.*, 2013, **73**, 1–16.

36 R. G. Bryant, *J. Chem. Educ.*, 1983, **60**, 933–935.

37 J. Feeney, J. G. Batchelor, J. P. Albrand and G. C. K. Roberts, *J. Magn. Reson.*, 1979, **33**, 519–529.

38 Y. Zhao and D. G. Truhlar, *J. Chem. Phys.*, 2006, **125**, 194101.

39 D. M. Heinekey, M. H. Voges and D. M. Barnhart, *J. Am. Chem. Soc.*, 1996, **118**, 10792–10802.

40 B. E. Hauger, D. Gusev and K. G. Caulton, *J. Am. Chem. Soc.*, 1994, **116**, 208–214.

41 D. G. Gusev, A. B. Vymenits and V. I. Bakhmutov, *Inorg. Chem.*, 1992, **31**, 1–2.

42 M. Mediati, G. N. Tachibana and C. M. Jensen, *Inorg. Chem.*, 1990, **29**, 3–5.

43 D. G. Gusev, V. I. Bakhmutov, V. V. Grushin and M. E. Vol'pin, *Inorg. Chim. Acta*, 1990, **177**, 115–120.

44 K. Zhang, A. A. Gonzalez and C. D. Hoff, *J. Am. Chem. Soc.*, 1989, **111**, 3627–3632.

45 A. A. Gonzalez, K. Zhang, S. P. Nolan, R. Lopez de la Vega, S. L. Mukerjee, C. D. Hoff and G. J. Kubas, *Organometallics*, 1988, **7**, 2429–2435.

46 D. E. Prokopchuk, E. S. Wiedner, E. D. Walter, C. V. Popescu, N. A. Piro, W. S. Kassel, R. M. Bullock and M. T. Mock, *J. Am. Chem. Soc.*, 2017, **139**, 9291–9301.

47 P. L. Holland, *Dalton Trans.*, 2010, **39**, 5415–5425.

48 C. Tsay and J. C. Peters, *Chem. Sci.*, 2012, **3**, 1313–1318.

49 J. L. Sudmeier, J. L. Evelhoch and N. B. H. Jonsson, *J. Magn. Reson.*, 1980, **40**, 377–390.

50 D. S. Stephenson and G. Binsch, *J. Magn. Reson.*, 1978, **32**, 145–152.

51 T. Le-Husebo and C. M. Jensen, *Inorg. Chem.*, 1993, **32**, 3797–3798.

52 D. C. Grills, R. van Eldik, J. T. Muckerman and E. Fujita, *J. Am. Chem. Soc.*, 2006, **128**, 15728–15741.

53 K. M. Gramigna, D. A. Dickie, B. M. Foxman and C. M. Thomas, *ACS Catal.*, 2019, **9**, 3153–3164.

54 W. H. Harman and J. C. Peters, *J. Am. Chem. Soc.*, 2012, **134**, 5080–5082.

55 R. C. Cammarota, L. J. Clouston and C. C. Lu, *Coord. Chem. Rev.*, 2017, **334**, 100–111.

56 S. Grimme, J. Antony, S. Ehrlich and H. Krieg, *J. Chem. Phys.*, 2010, **132**, 154104–154122.

57 Y. Zhao and D. G. Truhlar, *Theor. Chem. Acc.*, 2008, **120**, 215–241.

58 L. Zhao, M. von Hopffgarten, D. M. Andrada and G. Frenking, *Wiley Interdisc. Rev.: Comput. Mol. Sci.*, 2018, **8**, e1345.

59 M. P. Mitoraj, A. Michalak and T. Ziegler, *J. Chem. Theory Comput.*, 2009, **5**, 962–975.

60 R. D. Shannon, *Acta Crystallogr., Sect. A: Cryst. Phys., Diffr., Theor. Gen. Crystallogr.*, 1976, **32**, 751–767.

61 M. V. Vollmer, J. Xie, R. C. Cammarota, V. G. Young, E. Bill, L. Gagliardi and C. C. Lu, *Angew. Chem., Int. Ed.*, 2018, **57**, 7815–7819.

62 D. D. Perrin, *Ionisation Constants of Inorganic Acids and Bases in Aqueous Solution*, Pergamon Press, Elmsford, NY, 2nd edn, 1982.

63 E. Y. Tsui, R. Tran, J. Yano and T. Agapie, *Nat. Chem.*, 2013, **5**, 293–299.

64 D. You and F. P. Gabbaï, *Trends in Chemistry*, 2019, DOI: 10.1016/j.trechm.2019.03.011.

65 A. Amgoune and D. Bourissou, *Chem. Commun.*, 2011, **47**, 859–871.

66 B. Cordero, V. Gómez, A. E. Platero-Prats, M. Revés, J. Echeverría, E. Cremades, F. Barragán and S. Alvarez, *Dalton Trans.*, 2008, **21**, 2832–2838.

67 J. Ye, R. C. Cammarota, J. Xie, M. V. Vollmer, D. G. Truhlar, C. J. Cramer, C. C. Lu and L. Gagliardi, *ACS Catal.*, 2018, **8**, 4955–4968.

68 P. A. Rudd, S. Liu, L. Gagliardi, V. G. Young and C. C. Lu, *J. Am. Chem. Soc.*, 2011, **133**, 20724–20727.

69 L. Krause, R. Herbst-Irmer, G. M. Sheldrick and D. Stalke, *J. Appl. Crystallogr.*, 2015, **48**, 3–10.

70 G. M. Sheldrick, *Acta Crystallogr., Sect. A: Found. Crystallogr.*, 2008, **64**, 112–122.

71 G. M. Sheldrick, *Acta Crystallogr., Sect. C: Struct. Chem.*, 2015, **71**, 3–8.

72 *Persistence of Vision (TM) Raytracer*, Persistence of Vision Pty. Ltd., Williamstown, Victoria, Australia, 2004.

73 Z.-L. Xue, A. J. Ramirez-Cuesta, C. M. Brown, S. Calder, H. Cao, B. C. Chakoumakos, L. L. Daemen, A. Huq, A. I. Kolesnikov, E. Mamontov, A. A. Podlesnyak and X. Wang, *Eur. J. Inorg. Chem.*, 2019, 1065–1089.

74 J. Zikovsky, P. F. Peterson, X. P. P. Wang, M. Frost and C. Hoffmann, *J. Appl. Crystallogr.*, 2011, **44**, 418–423.

75 A. J. Schultz, M. R. V. Jorgensen, X. Wang, R. L. Mikkelson, D. J. Mikkelson, V. E. Lynch, P. F. Peterson, M. L. Green and C. M. Hoffmann, *J. Appl. Crystallogr.*, 2014, **47**, 915–921.

76 A. J. Schultz, K. Srinivasan, R. G. Teller, J. M. Williams and C. M. Lukehart, *J. Am. Chem. Soc.*, 1984, **106**, 999–1003.

77 A. Thorn, B. Dittrich and G. M. Sheldrick, *Acta Crystallogr., Sect. A: Found. Crystallogr.*, 2012, **68**, 448–451.

78 C. R. Yonker and J. C. Linehan, *Prog. Nucl. Magn. Reson. Spectrosc.*, 2005, **47**, 95–109.

79 C. R. Yonker and J. C. Linehan, *J. Organomet. Chem.*, 2002, **650**, 249–257.

80 P. H. M. Budzelaar, *gNMR User Manual, 5.0*, IvorySoft, 2006.

81 M. J. Frisch, G. W. Trucks, H. B. Schlegel, G. E. Scuseria, M. A. Robb, J. R. Cheeseman, G. Scalmani, V. Barone, B. Mennucci G. A. Petersson, *Gaussian 09, Revision E. 01*, Gaussian, Inc., Wallingford CT, 2009.

82 C. Adamo and V. Barone, *J. Chem. Phys.*, 1999, **110**, 6158–6170.

83 D. Andrae, U. Haeussermann, M. Dolg, H. Stoll and H. Preuss, *Theor. Chim. Acta*, 1990, **77**, 123–141.

84 F. Weigend and R. Ahlrichs, *Phys. Chem. Chem. Phys.*, 2005, **7**, 3297–3305.

85 A. V. Marenich, C. J. Cramer and D. G. Truhlar, *J. Phys. Chem. B*, 2009, **113**, 6378–6396.

86 *ADF2016, SCM, Theoretical Chemistry*, Vrije Universiteit, Amsterdam, The Netherlands, http://www.scm.com.

87 G. te Velde, F. M. Bickelhaupt, E. J. Baerends, C. Fonseca Guerra, S. J. A. van Gisbergen, J. G. Snijders and T. Ziegler, *J. Comput. Chem.*, 2001, **22**, 931–967.

88 E. Van Lenthe and E. J. Baerends, *J. Comput. Chem.*, 2003, **24**, 1142–1156.

89 E. Van Lenthe, J. Snijders and E. Baerends, *J. Chem. Phys.*, 1996, **105**, 6505–6516.

90 P. J. Hay and W. R. Wadt, *J. Chem. Phys.*, 1985, **82**, 299–310.

91 R. Krishnan, J. S. Binkley, R. Seeger and J. A. Pople, *J. Chem. Phys.*, 1980, **72**, 650–654.